American Mineralogist, Volume 81, pages 1301–1314, 1996

The electronic structure of hematite {001} surfaces: Applications to the interpretation of STM images and heterogeneous surface reactions

UDO BECKER,[1,*] MICHAEL F. HOCHELLA JR.,[1] AND EDOARDO APRÀ[2]

[1]Department of Geological Sciences, Virginia Polytechnic Institute and State University, Blacksburg, Virginia 24061-0420, U.S.A.
[2]Pacific Northwest Laboratories, Battelle Boulevard, MS K1-90, Richland, Washington 99352, U.S.A.

ABSTRACT

Scanning tunneling microscope (STM) images and scanning tunneling spectroscopy (STS) spectra of hematite (α-Fe_2O_3) surfaces were calculated using ab-initio methods, not only to interpret experimentally collected STM data, but also to gain insight into atomic level changes in electronic structure that are associated with heterogeneous surface reactions.

The electronic structure and wave functions inside the studied crystal were obtained as a periodic solution of the Schrödinger equation by using the program Crystal92. STM images and STS spectra were calculated by applying a technique similar to the Tersoff and Hamann (1985) method.

Experimental STM images of the upper valence band of hematite (001) surfaces, cleaved in air, show a periodic array of bright spots that differs slightly from the O-O separation in the bulk. However, our calculations show that these spots are located at the Fe positions of the surface Fe atoms and above the Fe atoms between the first and second hexagonally close-packed O layers. The calculated STS spectra for tip positions above the three nonequivalent Fe positions show significant differences, in particular because the contribution of O 2p-like and Fe 3d-like states changes with the distance between the tip and the respective Fe atom underneath.

Hematite crystals that were used to obtain STM images experimentally in previous studies were cleaved in air, and the presence of adsorbed H_2O and O_2 was considered in this study. Calculations that optimize the surface atomic arrangement with respect to total energy of the slab indicate that H_2O and O_2 adsorbed to the surface have binding energies too low to withstand the dragging force and the electric potential applied during the scanning process. In addition, only calculations of STM images of fresh hematite surfaces exactly mimic the periodicity of high electronic density spots, as observed in experiments.

STS spectra calculated for equivalent Fe positions on terraces and near steps show the increased electron density of the top of the valence band for step sites, which is experimentally observed as higher intensities of bright spots at steps.

These calculations show that the local electronic structure of surfaces can be very different from bulk electronic properties and that conclusions drawn from cluster calculations representing the bulk can be misleading. In addition, this theoretical approach helps to explain the increased reactivity at specific sites on hematite, such as steps and kinks, in terms of the electronic surface structure of this mineral.

INTRODUCTION AND BACKGROUND

The electronic structure of hematite (α-Fe_2O_3) has been studied over the years (e.g., Tossell et al. 1973, 1974; Sherman 1985; Fujimori et al. 1987) to permit interpretation of XPS and UPS spectra (e.g., Kurtz and Henrich 1983, 1987; Lad and Henrich 1989a, 1989b; Ciccacci and De Rossi 1991), X-ray fluorescence spectra (e.g., Kawai et al. 1994), X-ray emission and absorption spectra (Drager et al. 1992), and ultraviolet and infrared absorption spectra (e.g., Sherman and Waite 1985), and to understand the bonding mechanisms and magnetic properties of iron oxides (e.g., Vaughan and Tossell 1978; Tossell and Vaughan 1992; Henrich and Cox 1994). These studies provide information about bulk properties and surface properties averaged over relatively large volumes and surface areas. However, surface reactions often occur in a highly nonuniform way across the surface (e.g., Hochella 1990, 1994). For instance, Junta and Hochella (1994) found that aqueous Mn^{2+} oxidizes and precipitates on hematite {001} surfaces starting at steps before manganese oxides grow from these sites to eventually cover the ter-

* Present address: Institut für Mineralogie, Universität Münster, Corrensstr. 24, D-48149 Münster, Germany.

0003–004X/96/1112–1301$05.00

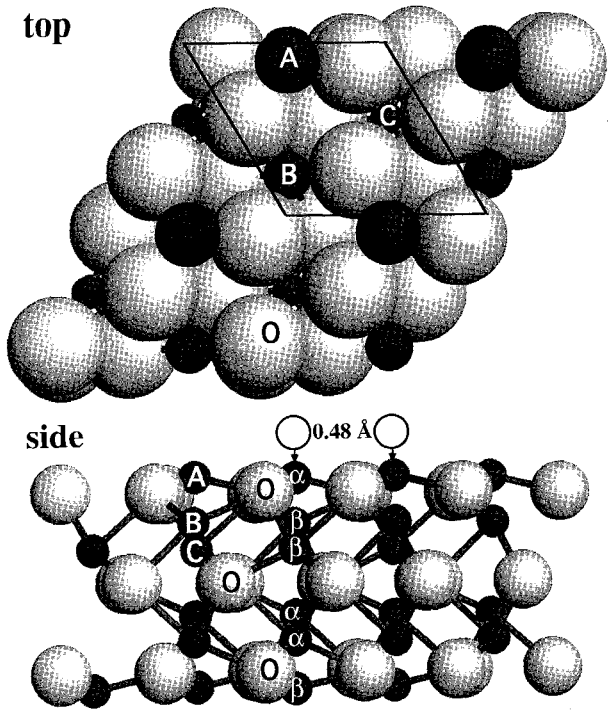

FIGURE 1. Top and side views of a hematite surface-slab model with relaxed surface atoms. This slab was used for Crystal92 calculations. The side view represents the actual thickness of the slab used for the calculations. The slab is infinite perpendicular to the [001] axis (i.e., to the left, right, top, and bottom in the top view). The labels A, B, and C stand for Fe^1_{low}, Fe^2_{high}, and Fe^2_{low}, respectively. The top view shows nonequivalent Fe atoms with varying sizes depending on their distance from the surface (Fe^1_{low} being the largest, Fe^2_{low} the smallest). The symbols α and β in the side view represent the spin symmetry of the antiferromagnetic spin configuration. The side view also shows the most significant relaxation feature, which is the Fe^1_{low} atoms being attracted toward the center of the slab by 0.48 Å.

races completely. This is a good example of why it is necessary to examine experimentally and theoretically the electronic structure of flat surfaces and to compare them with specific sites, such as steps, kinks, and defects. With the knowledge of the properties of these sites, it may be easier to predict environmentally relevant metal-partitioning reactions, e.g., for the removal of metals from surface or ground waters. These reactions are also important for the purification of drinking water (e.g., Knocke et al. 1990). In addition, studies of the electronic and magnetic surface structures of iron oxides can help to explain the properties of iron oxides used in magnetic data-storage devices (Masai et al. 1994).

Only a few studies have been performed to image iron oxide surfaces at an atomic or near-atomic level using scanning tunneling microscopy (STM) (Zeng-Jun and Jun-Jue 1992; Eggleston and Hochella 1992; Eggleston et al. 1992; Eggleston and Stumm 1993; Masai et al. 1994; Condon et al. 1994; Lennie et al. 1996). However, interpretations of these images have remained ambiguous because the assignment of sites with high electronic density in the upper valence band to particular atoms or to specific atomic orbitals had to be deduced from cluster or bulk molecular orbital (MO) calculations (e.g., Sherman 1985; Fujimori et al. 1986, 1987). Some assignments were undertaken by comparing the periodicity of bright spots in the experimental STM image to the periodicity of atoms in the unrelaxed surface geometry.

In this study, we present calculations of STM images of hematite {001} surfaces that can be directly compared with experimentally obtained images. If theoretical STM images are compared with experimental images collected in air, the presence of adventitious material must be taken into account. It is known from previous XPS studies that adventitious O_2, H_2O, and C can be found on hematite parting planes that are exposed to air (Junta-Rosso and Hochella 1996). These layers usually have a thickness of approximately 10 Å. Therefore, these calculations had to clarify whether the observed periodic arrays of bright spots represent orbitals of atoms that belong to the hematite surfaces or orbitals from adsorbed O_2 or H_2O.

We also calculated scanning tunneling spectra (STS) that can serve as characteristic patterns for future measurements to analyze more precisely the electronic structure of single atoms. By comparing these calculated STS spectra with future measurements of experimentally obtained STS spectra, single atomic sites or adsorbed structures in geologic samples may be unambiguously identified at an atomic scale for the first time. Experimental STS spectra were obtained by stopping the scanning process over certain atomic positions of the sample and ramping the bias voltage over a selected voltage range, e.g., from −2 to +2 V. In this example, electronic information would be obtained for the uppermost 2 eV of the valence band and the bottom 2 eV of the conduction band of the sample underneath the tip termination. For example, Avouris and Lyo (1991) were able to resolve the mechanism of back bonding during oxidation of Si surfaces by comparing calculated and experimental STS spectra.

In addition, the combination of STM, STS, and MO calculations is the only method that can monitor electron transfer at an atomic level. Therefore, it is the most promising approach for obtaining insight into the nonuniform character of surface redox reactions that are influenced by several complex surface sites such as terraces, steps, kinks, vacancies, and impurities.

CRYSTAL STRUCTURE OF HEMATITE

To explain relaxation features of surface slabs, we briefly describe the bulk structure of hematite. Hematite has the corundum (α-Al_2O_3) structure (space group $R\bar{3}c$, with six formula units in the conventional hexagonal unit cell). Its structure consists of slightly distorted, hexagonal close-packed {001} layers of O atoms (O-O separations of 2.6 and 3.1 Å), with Fe atoms filling two-thirds of the octahedral sites (as shown in Fig. 1). Described in terms

of a layered or slab structure parallel to the {001} face, there are two Fe layers between each hexagonal close-packed layer of O atoms. These two layers are 0.64 Å apart, and the {001} parting plane is between these two Fe layers. Fe atoms in the upper Fe layer are labeled with the subscript "high," in the lower with "low." The superscript indicates between which O layers the Fe atom can be found. With this nomenclature, Fe^{1}_{low} is the Fe atom above the uppermost O layer, and Fe^{2}_{high} and Fe^{2}_{low} are the Fe atoms in the two Fe layers between the first and second O layer. In each hexagonal surface unit cell on a parting plane, there is one surface Fe^{3+} atom (Fe^{1}_{low}) and three O atoms (Fig. 1).

The bulk structure was refined by Sato and Akimoto (1979) from X-ray diffraction data. These data were used in this study for MO calculations of the bulk.

Computational methods

To calculate the electronic structure within the sample, the program Crystal92 (Dovesi et al. 1994) was used. This program calculates wave functions for periodic structures that are infinite (in x and y) slabs in the case of modeling surfaces. The periodicity of the slab is obtained from a surface unit cell by solving the Coulomb and exchange integrals in the Hartree-Fock (HF) approach for treating the Schrödinger equation in reciprocal space (for a review, see Pisani et al. 1988). For all geometry optimizations, Pople-type 3-21g* basis sets were used with a 41g basis set for calculating Fe 3d orbitals. The contraction set for the inner valence electrons was split, and the exponents for the outer valence functions were optimized for the bulk geometry as determined by Sato and Akimoto (1979). For geometry optimizations, we implemented a program written by Becker (1995a) that uses Crystal92 and a combination of a Newton-Raphson algorithm and a quadratic convergence approach to minimize the total energy of a periodic structure.

The method for calculating STM images, STS spectra, and projected STS spectra is described in Becker (1995b, 1995c) and Becker and Hochella (1996). Projected STS spectra were obtained by multiplying a wave function (Ψ) with only the contributions of those atomic orbitals (e.g., $\Psi_{Fe\ 3d}$, for projections onto Fe 3d) onto which it is projected, instead of calculating $|\Psi|^2$ for the evaluation of the charge density of an orbital. In this way, the contribution of, for example, Fe 3d orbitals to STM images or STS spectra can be separated.

For the calculation of STM images, special care must be taken with the diffuse Gaussian functions of each basis set to obtain reliable results for the vacuum tail of the wave function. Therefore, the diffuse basis functions were modified by a method described in Becker and Hochella (1996). However, the use of very diffuse functions is computationally and disk-space intensive in the reciprocal space approach. Therefore, it was necessary to simplify the role of the O and Fe ion cores by applying the pseudopotential theory, which allows the use of valence-only basis sets. The pseudopotential method approximates the molecular orbitals of the inner shells as an electrostatic field of screened ion cores with radial symmetry. This is legitimate because the inner shells of these atoms are relatively undisturbed by their own valence electrons and those of the coordinating atoms. Hay and Wadt–type large-core pseudopotentials (Hay and Wadt 1985) were used.

The hematite slab used in this study was three close-packed O layers thick (see side view, Fig. 1) with three O atoms per surface unit cell and layer (see top view, Fig. 1). There are two Fe layers, labeled B ("high" position) and C ("low" position), in between each O layer, and an Fe layer on the top (labeled A, in "low" position) and bottom (in "high" position) of the slab. Each Fe layer contains only one Fe atom per surface unit cell. The chosen slab was thick enough to mimic bulk-like conditions in the middle of the slab, where relaxation features do not extend. In addition, slab thickness was limited by the cost of the computations, which formally increase with the fourth power of the number of electrons (in practice, efficient screening criteria reduce this cost to a quadratic scaling). A slab too thick would therefore require undesirable compromises in computational precision. The argument that the slab thickness was sufficient to mimic the main relaxation features is further justified in the section on the atomic structure of relaxed hematite (see below).

Because typical tip-sample separations are on the order of 4–10 Å, and STM images can vary with the tip-sample separation within the first few angstroms above the sample surface (one example is given in the Results and Discussion section below), it is crucial to approximate the vacuum region as well as possible. Therefore, in addition to using the methods described in Becker and Hochella (1996) to calculate the electronic structure within the surface slab, a grid of ghost atoms was put between the surface and the tip. Ghost atoms are symmetry centers for basis functions, but they do not have a nuclear charge. Such a grid was necessary because the charge-density dropoff from the sample surface into the vacuum is overestimated by the periodic HF approach using Gaussian functions (Becker and Hochella 1996). In addition, because of the overestimated charge-density dropoff of the sample, we chose tip-sample separations of 4 Å in most cases, i.e., near the lower end of the ones typically applied (for a particular experimental image, the tip-sample separation is never exactly known, but it can be assumed to be low because hematite is a wide-band-gap semiconductor). Because of the structure of hematite, orbitals of Fe atoms as far down as the second close-packed O layer can potentially contribute to bright spots of high electronic density in STM images because none of these Fe atoms (Fe^{1}_{low}, Fe^{2}_{high}, Fe^{2}_{low}) is covered by the uppermost O layer. The application of a grid of ghost atoms helps to minimize the underestimation of the electronic density that stems from orbitals of atoms that lie deeper below the surface. The ghost-atom approach has typically been used to create additional basis-function centers to repre-

TABLE 1. Surface relaxation, binding energies, and bond distances of freshly parted hematite and hematite surfaces with H_2O or O_2 adsorbed to them

	Freshly parted hematite	H_2O adsorbed	O_2 adsorbed
Relaxation of uppermost Fe (Fe^1_{low})	0.48 Å	0.30 Å	0.48 Å
Binding energy of adsorbed molecule	N/A	11.8 kcal/mol* = 0.5 eV/molecule* ≈0.7 eV/molecule**	≈0.2 eV/molecule**
Fe^1_{low}-adsorbed molecule distance	N/A (closest bond distance in bulk hematite: 1.88 Å)	2.25 Å	2.51 Å

* Hendewerk et al. (1986), from desorption experiments.
** This study.

sent valence orbitals better within and around an atomic cluster (e.g., Latajka and Scheiner 1989). In this study, we used a grid of ghost atoms in the vacuum gap because extremely diffuse functions cannot be handled by the periodic HF approach.

The ghost-atom grid was positioned about 1 Å above the surface. This distance could be varied in only a small range. Smaller separations between the surface and ghost atoms lead to undesirable basis-set superpositions and thereby an overestimation of the lattice energy near the surface. Larger separations would result in wave functions that drop off from the sample and increase again toward the ghost-atom grid. Also, in both of these cases, the solution of the HF approach usually does not converge. Laterally, ghost atoms were uniformly distributed to avoid artifacts resulting from ghost-atom positioning. In addition, ghost atoms preferably should be located on symmetry axes, such that the symmetry of the slab (which has the same symmetry properties as any observable, such as an STM image) is preserved. Therefore, we put ghost atoms on the threefold symmetry axes, of which there are three per unit cell perpendicular to the {001} surface. Another ghost-atom grid with twice the ghost-atom density (one-half the ghost-atom–ghost-atom separation, which still preserves the symmetry) was applied for comparison but did not significantly change the wave function in the vacuum. Each ghost atom was the center of a diffuse s, p, and d basis function, with the same Gaussian exponent ($\alpha = 0.18$) on each of them. This exponent and the distance between the ghost-atom grid and the mineral surface was optimized with respect to total slab energy.

The ghost-atom grid cannot be used if STS spectra are compared with their projections onto certain orbitals to get orbital character information, as was done in this study. This is because the ghost-atom orbitals mix the information of different atomic orbitals. For instance, an s orbital of a ghost atom would correct for the vacuum tail of Fe 4s and O 2s orbitals; therefore, the contribution of the orbitals to a particular spectrum could not be separated by using the projection method. However, if the ghost-atom grid is omitted in the calculation, the intensities of calculated spectra are unreliable, whereas the shape of the spectra stays fairly constant. Therefore, the intensities of STS spectra presented in this study can be compared only with the intensities of their projections, not with the intensities of STS spectra calculated for different tip positions with varying distances between the tip and the closest surface atom.

Different antiferromagnetic spin configurations were tested to find the energetically most favorable one. In agreement with bulk calculations by Catti et al. (1995), this study used the optimized spin configuration for surfaces shown in Figure 1 (α = spin ↑, β = spin ↓).

RESULTS AND DISCUSSION

Relaxation of fresh hematite surfaces and surfaces with adsorbed H_2O and O_2

Relaxation of fresh hematite surfaces and surfaces with H_2O or O_2 adsorbed to them were studied to clarify the effect of relaxation on the electronic structure and STM images. In addition, these studies give insight into the bond energies of adsorbed species and the ability of adsorbate structures to restore the coordination sphere of surface Fe^{3+}. Table 1 summarizes the results of the calculated relaxation. The most significant relaxation feature of fresh hematite surfaces is that the uppermost Fe atom (Fe^1_{low} in Fig. 1) is pulled toward the surface by 0.48 Å after parting because of the loss of three Fe-O bonds (in bulk hematite, Fe^{3+} is bonded octahedrally to six O atoms). As can be seen in Figure 1, the surface Fe atoms lie almost in the outermost plane of O atoms. This process shortens the bond length only from 1.88 to 1.77 Å because the first O plane relaxes by 0.07 Å toward the next O plane. In addition, there is a lateral relaxation in the uppermost O plane because the top surface Fe atom (Fe^1_{low}) being pulled toward the surface pushes the surface O atoms surrounding it 0.014 Å to the side. The contraction of the surface metal ion toward the bulk and the lateral relaxation of the O atoms in the uppermost O layer compare well with similar relaxation features that have been calculated for isostructural corundum (see, e.g., Causà et al. 1988; Manassidis et al. 1993). Fe atoms between the first and second O layers (Fe^2_{high} and Fe^2_{low} in Fig. 1) relax by only 0.03 and 0.01 Å toward the center of the slab. These small relaxation values one monoatomic layer down from the surface show that the slab thickness for our calculations as represented in the side view of Figure 1 is sufficient to capture the depth where significant surface relaxation takes place.

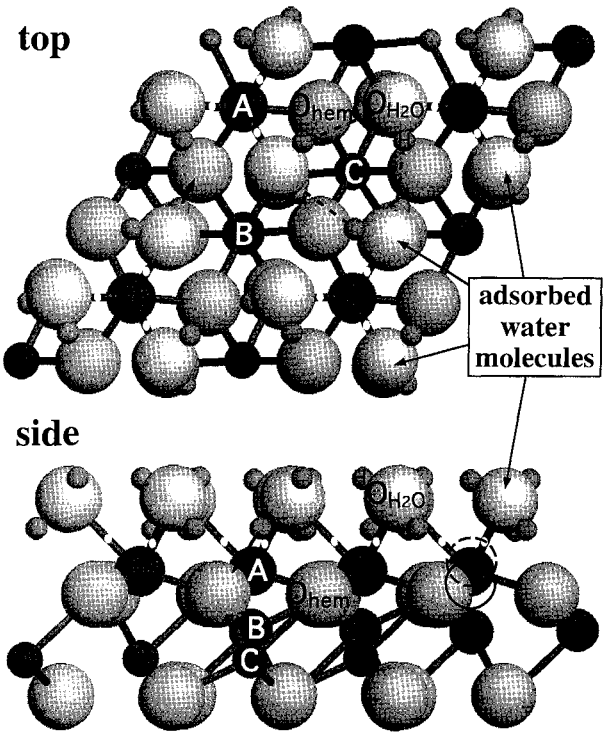

FIGURE 2. Top and side views of a hematite surface-slab model with adsorbed H_2O, optimized using Crystal92 and an optimizer by Becker (1995a) (based on an optimizer by Towler 1993, only the upper half of the slab is shown). Labels A, B, and C as in Figure 1. Adsorbed H_2O restores the octahedral coordination sphere of Fe^{I}_{low} (these relatively weak bonds are indicated by a white dot on the bond). If there were interaction only between the H_2O molecule and Fe^{I}_{low}, the negative pole of the H_2O dipole would point toward Fe^{I}_{low}. However, one of the H atoms always forms a hydrogen bond to another H_2O molecule that is bonded to a different Fe^{I}_{low} (three such hydrogen bonds are indicated by dashed lines in the top view). These hydrogen bonds can be seen as weak shadows in the theoretical STM image shown in Figure 12. The other H atom forms a weak hydrogen bond to an O atom on the hematite surface (one such bond is indicated by an arrow in the top view and the side view). In the side view, the position of Fe^{I}_{low} in the bulk is indicated by a dashed circle, and the position on a relaxed hematite surface by a solid circle. This shows how H_2O is able to pull Fe^{I}_{low} partially back to its original position in the bulk.

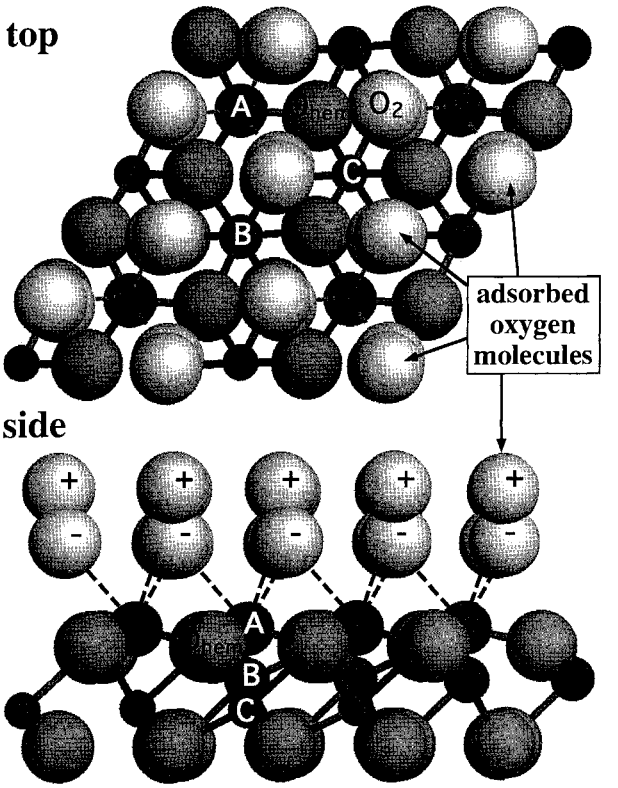

FIGURE 3. Top and side views of a hematite surface-slab model with adsorbed molecular O, optimized using Crystal92 (only the upper half of the slab is shown). Labels A, B, and C as in Figure 1. Adsorbed molecular O atoms are represented with lighter shading than O atoms incorporated into the hematite structure. In contrast to the binding mechanism of H_2O with a permanent dipole, the O atom in molecular O that is closer to the surface is negatively polarized, whereas the other has a partial positive charge.

It is interesting that during relaxation, the surface Fe atoms (Fe^{I}_{low}) almost completely restore their spin density from 3.8 in the unrelaxed case to 4.4 in the relaxed position. Bulk Fe atoms have a spin density of 4.6 according to a Mulliken population-density analysis, whereas an isolated Fe^{3+} ion ($3d^5$) has a spin density of 5. The different values are due to the partially covalent character of the Fe-O bond.

To study H_2O adsorption, we optimized the geometry of three H_2O molecules per surface unit cell of hematite because this is the maximum number of molecules that can be adsorbed to the surface within a monomolecular layer. With H_2O adsorbed to the surface, the octahedral coordination sphere of the top Fe^{3+} ion (Fe^{I}_{low}) is restored (Fig. 2), but the octahedron is very distorted. Because of the attractive force of the dipolar H_2O molecules, Fe^{3+} ions are only 0.3 Å closer to the underlying O layer relative to where they would be in the bulk structure. In other words, adsorption of H_2O withdraws Fe^{3+} ions by 0.18 Å with respect to the Fe^{I}_{low} position (which was contracted by 0.48 Å into the top O layer, Fig. 1) on the relaxed, fresh hematite surface (see side view in Fig. 2). Yet, the Fe-O_{H_2O} bond strength is weaker than the Fe-O bond strength in the bulk. This is observable as an increase in bond length (Fe-O_{H_2O} separation = 2.25 Å vs. Fe-O_{bulk} separation = 1.88 Å). The bond energy is about 0.7 ± 0.2 eV between one H_2O molecule and a surface Fe as calculated from the difference in energies of the slab with H_2O adsorbed and the isolated slab with isolated H_2O molecules. This bond energy is comparable to 0.5 eV (~50 $kJ/mol_{absorbed\ H_2O}$), as determined by desorption experiments of Hendewerk et al. (1986).

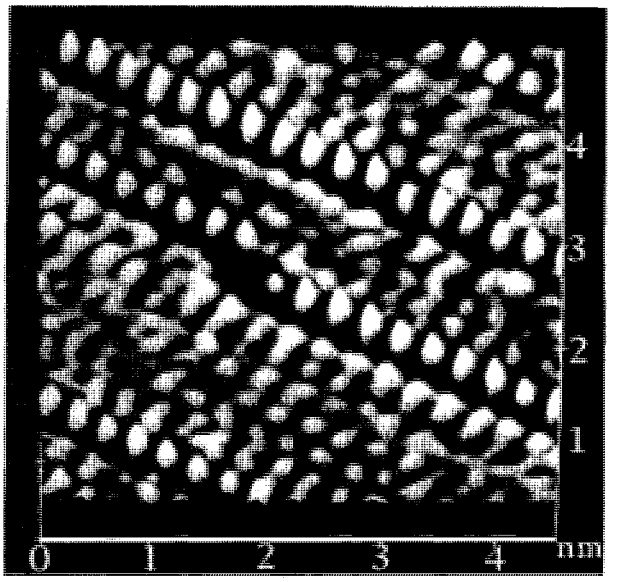

FIGURE 4. Experimental constant-height STM image, 54 × 54 Å, of a hematite {001} surface, taken at −0.3 V bias voltage and 1.5 nA setpoint current, showing monoatomic surface steps with spots of increased electronic valence-band density along the steps. The surface steps down from the top right to the bottom left. The height of each step is approximately 2.5 Å. The data are displayed in a three-dimensional block tilted 60° toward the viewer (from Eggleston and Hochella 1992).

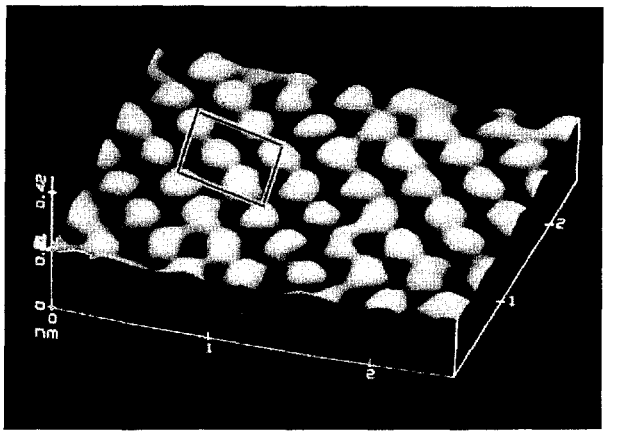

FIGURE 5. Experimental STM image of a hematite {001} parting plane showing a flat surface terrace, taken at −0.3 V bias voltage and 2.2 nA setpoint current. There are three spots of high valence-band density per unit cell in a hexagonal array with a uniform spot-spot separation of 2.95 Å. The hexagonal unit cell is slightly distorted because of drift effects (from Eggleston and Hochella 1992).

Adsorbed O_2 does not have a detectable influence on the surface topography of hematite (Fig. 3). The bond length Fe-O_{O_2} is about 2.5 Å, and the bond energy is about 0.2 eV.

Bond energies can be compared to bias voltages applied between tip and sample. Eggleston and Hochella (1992) applied negative bias voltages between −0.3 and −1.2 V (Figs. 4 and 5). The maximum applied bias voltage, with a corresponding electrical energy of −1.2 eV, especially can break bonds between the surface and adsorbate structures up to about that energy. A simple model of how this bond breaking occurs could be as follows: At a negative sample bias voltage, the negative end of the H_2O dipoles get turned away from the sample (these ends were originally pointing toward Fe^1_{low}) and the negative polarization of adsorbed O_2 molecules toward Fe^1_{low} gets overcompensated by the polarization toward the tip. In addition to the electric field induced by the tip, a mechanical dragging force can act on adsorbed molecules during the scanning process. Therefore, the applied electrical energy of 0.3–1.2 eV is likely to push most adsorbed O_2 molecules and at least some of the H_2O molecules away from the location of the tip, in the case in which H_2O or O_2 are adsorbed to the surface during exposure to air. This is the first hint that the bright spots in Figures 4 and 5 do not relate to adsorbed O_2 or H_2O even though they are present before the tunneling process (Junta-Rosso and Hochella 1996).

Electronic structure of fresh hematite surfaces

For the calculation of STM images and STS spectra, the most significant orbitals are those at the top of the valence band for negative bias voltages and at the bottom of the conduction band for positive bias voltages. In addition, this represents very well the energy range for electrons that can potentially take part in surface reactions.

Figure 6a shows the density of states (DOS) of a surface slab at the top of the valence band and the bottom of the conduction band. The DOS representation is projected onto Fe 3d states of the uppermost Fe layer (Fe^1_{low}, Fig. 6b), the Fe layer underneath the top O layer (Fe^2_{high}, Fig. 6c), and O 2p states of O atoms in the top O layer (Fig. 6d). It can be seen that the top of the valence band is formed by mixed Fe 3d and O 2p states with predominantly O 2p character. This is in agreement with previous results by Catti et al. (1995) for bulk hematite and with cluster calculations performed by Tossell et al. (1973, 1974) and Sherman (1985). These mixed states are due to ligand-to-metal charge transfer (LMCT), as already stated in studies using cluster calculations, IR and UV absorption spectra, and photoelectron emission spectra (Sherman and Waite 1985; Lad and Henrich 1989a, 1989b; Fujimori et al. 1987). Even though this pattern is also found in this study for surface slabs, it might be possible that HF calculations slightly underestimate the influence of LMCT and therefore overestimate the importance of O 2p states for the top of the valence band. This may be because with the use of the HF approach, electron redistribution from occupied O states to unoccupied Fe states (with respect to a completely ionic bonding mechanism) is hindered by the neglect of correlation effects.

The bottom of the conduction band is dominated by Fe 3d-like states. The bulk band gap of ~12.5 eV, as mod-

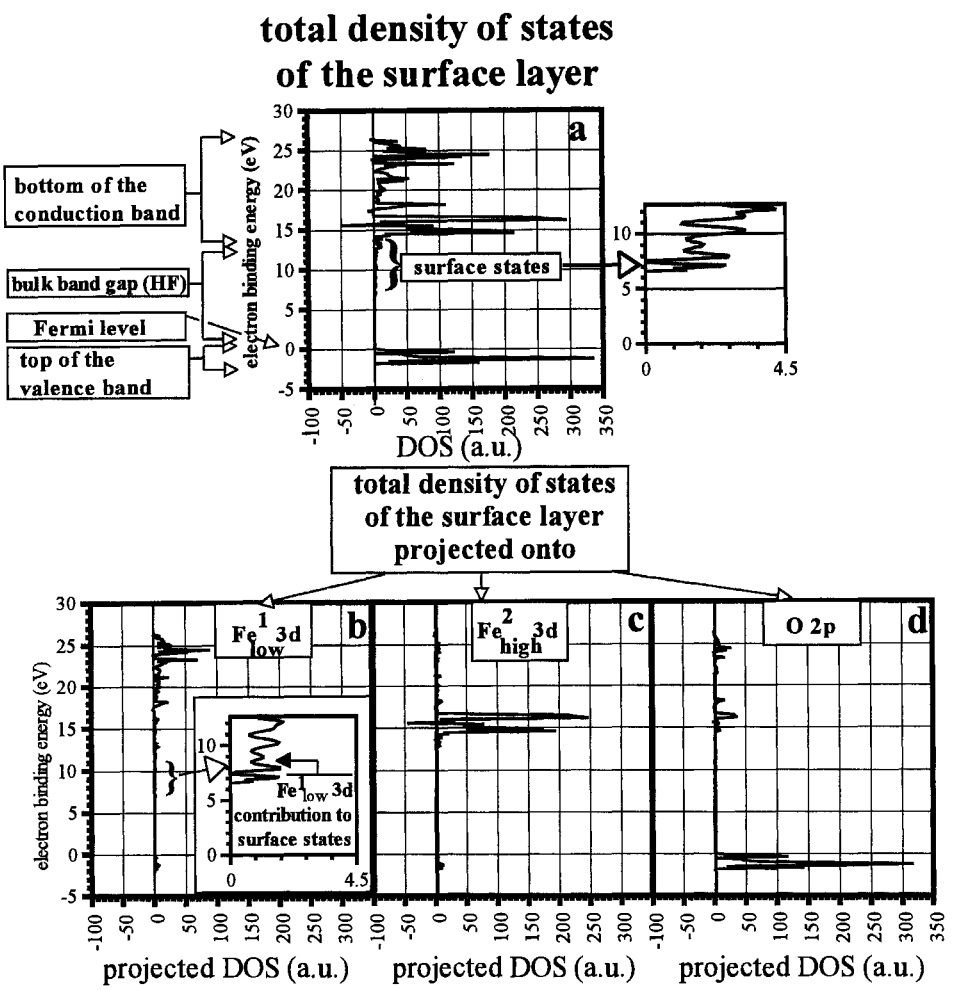

FIGURE 6. (**a**) Total density of states (DOS) of a hematite {001} surface layer with projections of the DOS onto (**b**) the 3d states of the uppermost Fe layer (Fe^1_{low}), (**c**) the 3d states of the Fe layer underneath the top O layer (Fe^2_{high}), and (**d**) the O 2p states of O atoms in the top O layer. HF surface-slab calculations result in a major contribution of O 2p states to the top of the valence band (compare **a** and **d** in the range between −3 and 0 eV). In contrast, the bottom of the conduction band is dominated by Fe 3d character, with Fe^1_{low} 3d creating the surface states in the bulk band gap between 5.5 and 12.5 eV (insets of **a** and **b**), and in **c** is represented by the projection onto Fe^2_{high} 3d.

eled by an infinite three-dimensional crystal, is greatly overestimated, as is typically observed for HF calculations. However, at the bottom of the conduction band of slabs (between +6.5 and +12.5 eV, Crystal92 calculates the Fermi level to be close to the top of the valence band, Fig. 6a), a small amount of electronic density is observed, which is best described as surface states (see insets of Figs. 6a and 6b). These states almost exclusively have Fe 3d character of the topmost Fe atoms (Fe^1_{low}, Fig. 6b). Even though the band gap is overestimated by HF calculations, the first empty states can be used as an estimate of the bottom of the conduction band (e.g., Becker and Hochella 1996).

Magnetic structure of fresh hematite surfaces

According to our calculations, the most energetically favorable spin configuration for surface slabs is antiferromagnetic, which is in agreement with earlier studies by Tasaki and Iida (1963) and Worlton et al. (1967). The antiferromagnetic structure reduces the space group of bulk hematite from $R\bar{3}c$ to $R\bar{3}$ because the Fe atoms are no longer equivalent. This is important because the spin configuration influences the electronic structure and calculated STS spectra (see next section). In addition, an understanding of the magnetic properties is relevant if iron oxides are considered as magnetic storage devices (e.g., Masai et al. 1994) or if magnetic force microscopy studies are performed on iron oxide surfaces (e.g., Williams et al. 1992; Lovlie 1993). In the antiferromagnetic spin configuration, the Fe atoms between two consecutive hexagonal close-packed (001) O layers have parallel spins, and the spin direction is opposite for the Fe atoms between the next two O layers. The stabilization energy

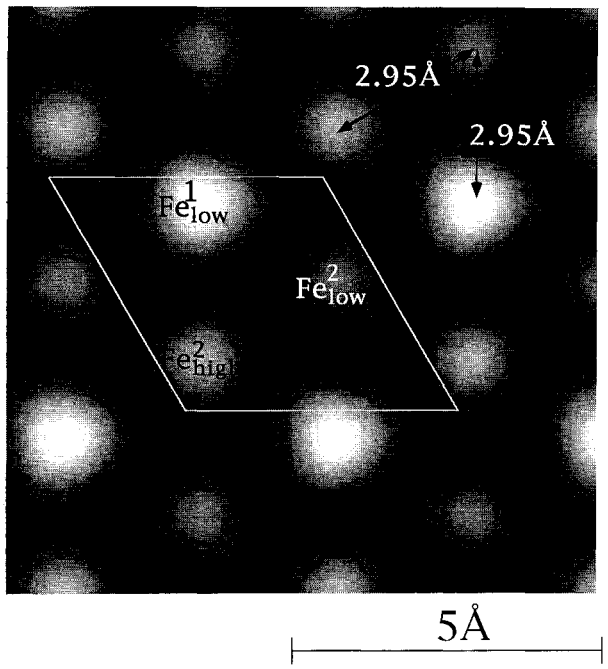

FIGURE 7. Calculated STM image of a hematite {001} surface at −0.3 V bias voltage (the shape of the image is relatively independent of the bias voltage in the range from −0.15 to −2 eV). Bright spots of high electronic valence-band density are located above Fe atoms (labeled Fe^1_{low}, Fe^2_{high}, and Fe^2_{low}, see Fig. 1) with varying contributions of states with Fe 3d and O 2p character (see Fig. 8 and text). A surface unit cell is outlined.

of the antiferromagnetic spin configuration in comparison with the ferromagnetic spin configuration is 0.0020 hartrees/Fe_2O_3 unit (0.0544 eV/Fe_2O_3 unit) for the relaxed surface. This value is of the same order as the antiferromagnetic stabilization energy of bulk hematite as determined by Catti et al. (1995; 0.0034 hartrees/Fe_2O_3 unit for HF, 0.0027 hartrees/Fe_2O_3 unit for HF after correcting for correlation effects).

Comparison of calculated STM images and STS spectra for fresh hematite surfaces with experimentally obtained images

The types of DOS calculations presented in the electronic structure section can provide us with electronic structure information averaged over the whole surface layer. However, for the calculation of STM images and STS spectra and for the study of the local distribution of reactive sites, the local density of states (LDOS) for each tip position above the sample must be examined. Two major factors determine the change between an averaged representation as in Figure 6 and an LDOS representation that is an approximation of an STS spectrum. The first factor is the geometry of the surface. For instance, one would expect a higher contribution of Fe 3d states for tunneling at negative bias voltages and tip positions on top of the uppermost Fe atom (labeled Fe^1_{low} in Fig. 1) because at these positions the distance between the tip and a surface Fe atom is minimal. The second factor is the degree of delocalization of atomic states. Tossell et al. (1974) stated that O 2p-like states are more localized than states with Fe 3d character, which suggests that the relative importance of Fe states might increase for the tunneling process that usually takes place in a range of about 4–10 Å of the vacuum gap between sample surface and tip.

Figure 7 shows the calculated STM image of a fresh hematite surface for a tip-sample separation of 4 Å and a bias voltage of −0.3 eV (images calculated for bias voltages ranging from 0.2 to −2.0 eV have very similar shapes even though the absolute value of the tunneling current varies significantly). The bright spots in Figure 7 are located above the Fe atoms that are labeled Fe^1_{low}, Fe^2_{high}, and Fe^2_{low} in Figure 1. Because these three Fe atoms are not equivalent, the three bright spots per surface unit cell do not have the same intensity in Figure 7.

This can be better understood if one analyzes the LDOS ($\propto$ STS spectra, Figs. 8a–8c) above the Fe atoms, which can also be projected onto certain states, analogous to the projection of the total DOS onto certain states (see previous section). From Figures 8d, 8g, and 8j, the projections of the STS spectrum for a tip position on top of Fe^1_{low} onto Fe^1_{low} 3d, Fe^1_{low} 4s, and O 2p states, respectively, it becomes clear that STS spectra taken above these topmost Fe atoms are mainly influenced by their 3d states (Fig. 8g). Only about 1% of such a spectrum has Fe 4s (Fig. 8g) character, and about 2% can be attributed to O 2p (Fig. 8j). In contrast, according to HF calculations, spectra taken above Fe^2_{high} and Fe^2_{low} atoms should have roughly 50% (compare Figs. 8b, 8e, and 8k) and 90% (compare Figs. 8c, 8f, and 8l) O 2p character, respectively. The main reason why these O 2p contributions cannot be detected as tunneling current intensity above O atoms is that these O 2p-like orbitals point toward the threefold symmetry axes that are located at the Fe positions. Therefore, at the position of the tip, tunneling current intensity can be detected only at these threefold axes having different combinations of states with Fe 3d and O 2p character. It is important to evaluate the percentage of Fe 3d character because electron transfer during surface reactions primarily takes place to and from Fe 3d states, in particular for redox reactions (e.g., Luther 1990). Also, adsorbed molecules tend to be oriented toward Fe^1_{low} atoms rather than Fe^2_{high} or Fe^2_{low} atoms (see Figs. 2 and 3 and the next section), although all three spots show similar valence-band densities on the STM image. Note that in contrast to the spectra, which always have positive values (STS spectrum $\propto$ LDOS $\propto |\Psi|^2$), the projected spectra can also have negative values (projected STS spectrum $\propto |\Psi \cdot \Psi^*_{\text{projected states}}|$, see Becker and Hochella 1996). STS spectra must be calculated without ghost-atom grids if they are to be compared with their respective projections (see Computational Methods section). Because neglect of the ghost-atom grid significantly affects the intensity of the spectra, and not so much the shape, the spectra in

Figures 8a–8c were normalized to give similar intensities for comparison (Figs. 8d, 8g, and 8j were normalized with the same factor as 8a; 8e, 8h, and 8k with the same factor as 8b; and 8f, 8i, and 8l with the same factor as 8c).

The nonequivalency of the three Fe atoms (Fe^1_{low}, Fe^2_{high}, Fe^2_{low}) cannot be detected as a significant difference in intensity of the three bright spots in one unit cell on the experimental image of a hematite terrace as shown in Figure 5. These differences might be exaggerated in the calculated image because of an incomplete correction for the overestimated wave-function dropoff into the vacuum by the ghost-atom method. This argument is supported by the fact that the differences in the calculated tunneling current above the three nonequivalent Fe atoms are even higher if no ghost-atom grid is applied between sample and tip. Another reason for the disagreement in the tunneling current variation between experiment and theory could be that the electric potential gradient resulting from the applied bias voltage was assumed to take place completely in the vacuum between sample and tip. This assumption is inherent by applying the Tersoff and Hamann (1985) theory. Part of this gradient could take place within the sample, which would result in a shift of electron density toward the surface (in the case of a negative sample bias). In this way, part of the intensity differences can be leveled by the electric potential gradient within the sample. Also, calculated STS spectra of the upper 3 eV of the valence band above these three Fe atoms show different patterns (Figs. 8a–8c). Therefore, in future experiments the STS spectra of neighboring Fe atoms could prove the nonequivalency of these sites with bright spots.

The interpretation that bright spots are located above Fe atoms explains the uniform spot-spot separation of 2.95 Å, which agrees with the experimental data of Eggleston and Hochella (1992, see also Fig. 5). They interpreted spots with high electronic density as being located above O atoms with predominantly O 2p character because the density of bright spots and their arrangement as a hexagonal close-packed pattern roughly agreed with the arrangement of O atoms in the uppermost O layer of a (001) surface. However, the O-O separation in such a layer in a bulk crystal varies from 2.6 to 3.1 Å, and a lateral relaxation on the order of 0.3 Å would be necessary to explain the uniform separation of the bright spots in the STM image of 2.95 Å. As described in the section on the relaxation of fresh hematite, the calculated lateral relaxation of O atoms is only 0.014 Å.

In contrast to the HF calculations presented in this study, some previous calculations that were based on configuration-interaction cluster calculations (e.g., Fujimori et al. 1987) have suggested that the very top of the valence band (approximately the uppermost 2 eV) has an almost exclusive Fe 3d character, but these calculations neglected surface-specific features. Future calculations that include correlation effects (e.g., by applying the density functional theory) and the specific atomic, electronic, and magnetic surface structure (as in this study) might be able to refine ligand-to-metal charge-transfer effects and correct the calculated spectra for these effects. Such a procedure might also result in slightly different ratios of Fe 3d and O 2p contributions to the calculated spectra. Understanding the orbital character of a mineral surface a few angstroms away from the surface can be very instructive because reactants approaching the mineral might react with only certain types of orbitals because of orbital symmetry restrictions.

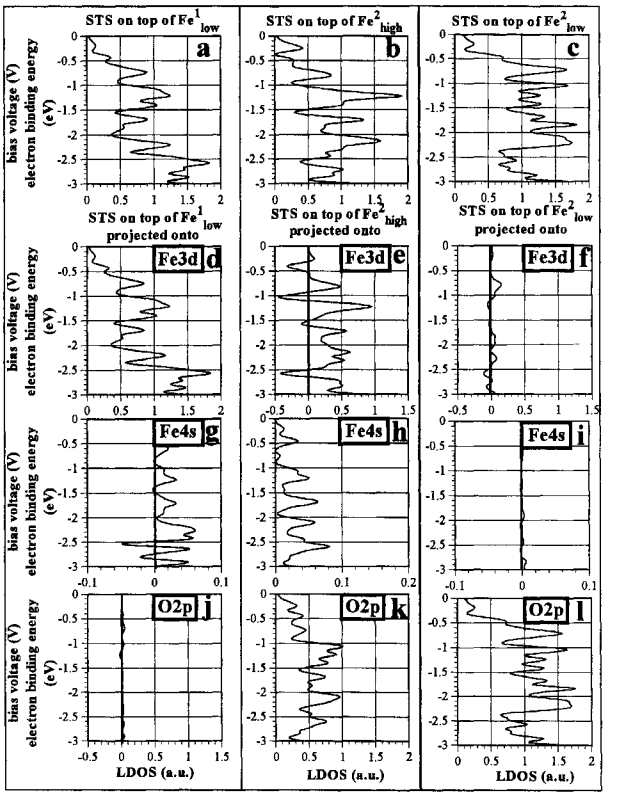

FIGURE 8. Calculated STS spectra for negative bias voltages between 0 and −3 V and their projections onto certain orbitals. The spectra were calculated for tip positions 4 Å away from the surface, above the Fe atoms Fe^1_{low} (**a**), Fe^2_{high} (**b**), and Fe^2_{low} (**c**). The spectra are projected onto the orbitals that contribute to the valence-band density at the respective positions. The STS spectrum of Fe^1_{low} (**a**) is projected onto Fe^1_{low} 3d (**d**), Fe^1_{low} 4s (**g**), and the O 2p orbitals (**j**). If the intensities of the projections (**d**, **g**, and **h**) are compared with the original calculated spectrum, it is obvious that spectra taken above Fe^1_{low} atoms have predominantly Fe^1_{low} 3d character. Analogously, the STS spectrum of Fe^2_{high} (**b**) is projected onto Fe^2_{high} 3d (**e**), Fe^2_{high} 4s (**h**), and the O 2p orbitals (**k**), and the STS spectrum of Fe^2_{low} (**c**) is projected onto Fe^2_{low} 3d (**f**), Fe^2_{low} 4s (**i**), and the O 2p orbitals (**l**). From Fe^1_{low} (O 2p character ≤10%), the O 2p character of the STS spectra increases about 50% at Fe^2_{high} (**k**) and >90% at Fe^2_{low} (**l**) because of decreasing Fe 3d character with increasing tip–Fe atom separation.

At positive bias voltages, Eggleston and Hochella (1992) observed variable images. Some contained only one bright spot per hexagonal unit cell, others featured triplets of spots of high conduction-band-state density

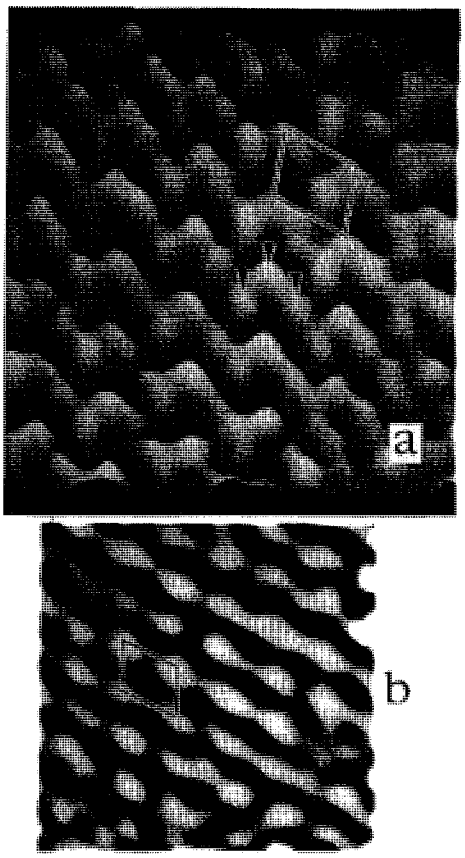

FIGURE 9. Experimental constant-height STM images of hematite {001} flat surfaces taken at positive bias voltages showing different features; both images were low-pass filtered to remove high-frequency noise. (**a**) STM image, 38 × 38 Å, taken at +1.05 V bias voltage and 5.2 nA setpoint current. Peaks occur in triplets (one such triplet is marked with arrows); the triplets occur in a hexagonal array with 5 Å periodicity. (**b**) STM image, 35 × 35 Å, taken at +1.1 V bias voltage and 3.8 nA setpoint current. Peaks occur in a hexagonal array with 5 Å periodicity, as expected for equivalent surface Fe (Fe^1_{low}) positions (both images from Eggleston and Hochella 1992).

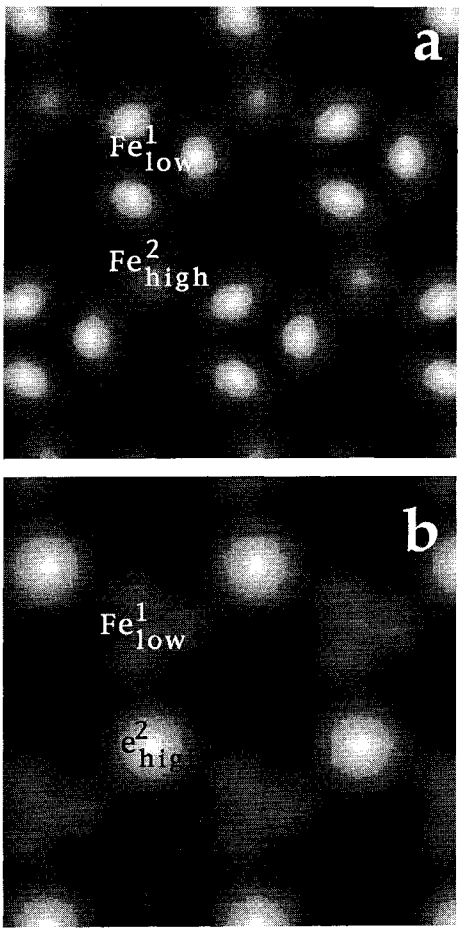

FIGURE 10. Calculated STM images, 10 × 10 Å, of hematite {001} flat surfaces at positive bias voltages for different tip-sample separations: (**a**) 2.5 Å, (**b**) 4.0 Å. The triplets in **a** might explain the triplets in Figure 9a (one such triplet per hexagonal unit cell), and the one bright spot per hexagonal surface unit cell (**b**) may be a good representation of the experimental image in Figure 9b.

(Fig. 9). One possible explanation for this observation is that the tip-sample separation was not constant for the different images collected. Therefore, we calculated STM images for a bias voltage of +1.1 eV, as in the experimental setup, and for tip-sample distances of 2.5 and 4.0 Å (Figs. 10a and 10b, respectively). The image calculated at 4 Å shows only one bright spot per hexagonal unit cell, and the one calculated for 2.5 Å represents the observed triplets. Differences in the tip-sample separation of experimental images could account for this variation. The image showing the triplets (Fig. 9a) was taken at a higher setpoint current (5.2 nA), and therefore smaller tip-sample separation, than the image (Fig. 9b) featuring just one spot per surface unit cell (3.8 nA). A setpoint current of, e.g., 1 nA means that the tip stops approaching the sample once the tunneling current reaches 1 nA for the bias voltage chosen. However, a decrease in the setpoint tunneling current of about 25% between the two experimental images usually does not account for a change in the tip-sample separation of 1.5 Å. Therefore, another argument in the observed variability of STM images at positive bias voltages has to be considered. If images are collected at different times, changes in the resistivity of mainly the tip can cause variations in the tip-sample separation. For instance, oxidation of the tip surface increases its resistivity, and for the same setpoint current the tip-sample separation would be decreased. This leads us to another possible explanation for the variability of experimental STM images at different bias voltages. Our calculations assume spherical tip wave functions as stated in the Tersoff and Hamann (1985) theory. However, as shown by Tsukada et al. (1991) and Kageshima and Tsukada (1992), the pattern seen on STM

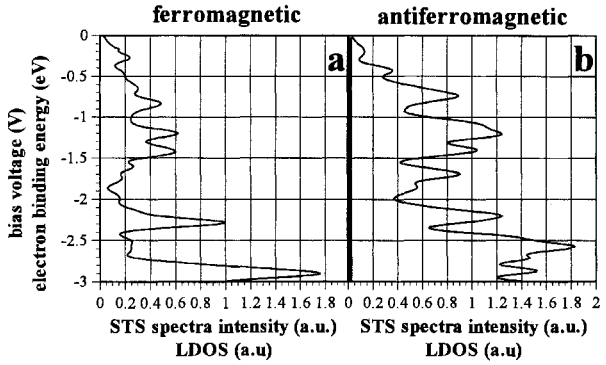

FIGURE 11. Calculated STS spectra for tip positions on top of Fe^1_{low} in the ferromagnetic (**a**) and antiferromagnetic (**b**) spin configurations. In both cases, the spin density of Fe^1_{low} (α-β spins) is the same, but the spin direction of the second Fe layer (Fe^2_{high} and Fe^2_{low}) is parallel to Fe^1_{low} in **a** and antiparallel to Fe^1_{low} in **b**.

images can depend on the atomic structure of the last tip atoms.

The location of these conduction band states is important for understanding redox reactions that involve electron transfer from a reductant to the hematite surface (e.g., Hering and Stumm 1990).

Figures 11a and 11b compare the calculated STS spectra for a tip position on top of Fe^1_{low} of the ferromagnetic and antiferromagnetic spin configurations. In both cases, the spin density of Fe^1_{low} (α-β spins) is the same, but we wanted to check whether the spin direction of the second Fe layer (parallel to Fe^1_{low} in the ferromagnetic case, antiparallel to Fe^1_{low} in the antiferromagnetic case) influences the local electronic structure on top of Fe^1_{low}. Comparison of Figures 11a and 11b reveals similarities between the two calculated spectra, such as the peaks at -0.8 and -2.2 V and the double peak between -1 and -1.5 V. However, significant differences must be noted, such as the absence of an LDOS peak at -1.7 V and differences in the intensity ratios of the peaks, e.g., the ratio between the double peak mentioned above and the peak at -1.7 V. Therefore, for a reliable calculation of STS spectra it is necessary to consider the local magnetic structure of the sample, in this case being antiferromagnetic (the most favorable spin configuration denoted by "α" and "β" in Fig. 1).

Calculated STM images of hematite surfaces with adsorbed H_2O or O_2

Even though, as stated above, the binding energy of H_2O or O_2 (approximately 0.6 and 0.2 eV, respectively) adsorbed to the surface is likely to be insufficient to withstand the tunneling process, we calculated STM images for these adsorbed structures to ensure that the experimental images truly represent fresh hematite surfaces. Figures 12 and 13 show the calculated STM images for

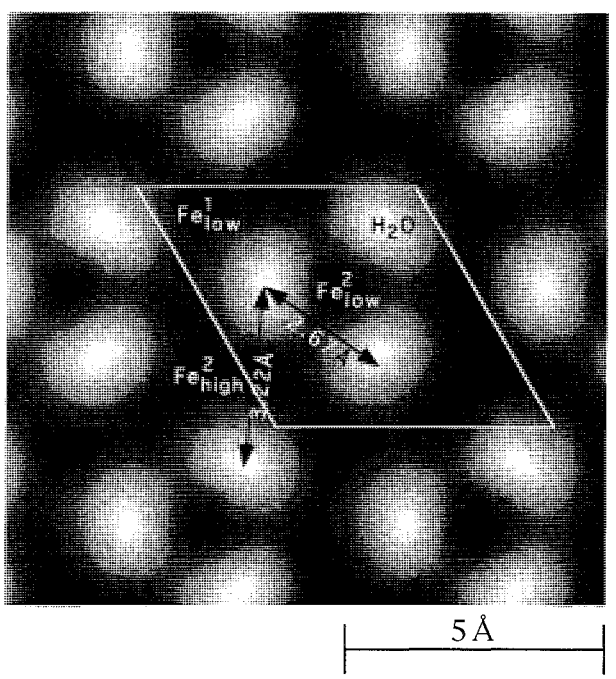

FIGURE 12. Calculated STM image of a hematite {001} surface with adsorbed H_2O (see Fig. 2), at -0.3 V bias voltage. Distances between bright spots vary from 2.67 to 3.22 Å, which is not in agreement with the experimentally observed uniform spot-spot separation of 2.95 Å (see Fig. 5).

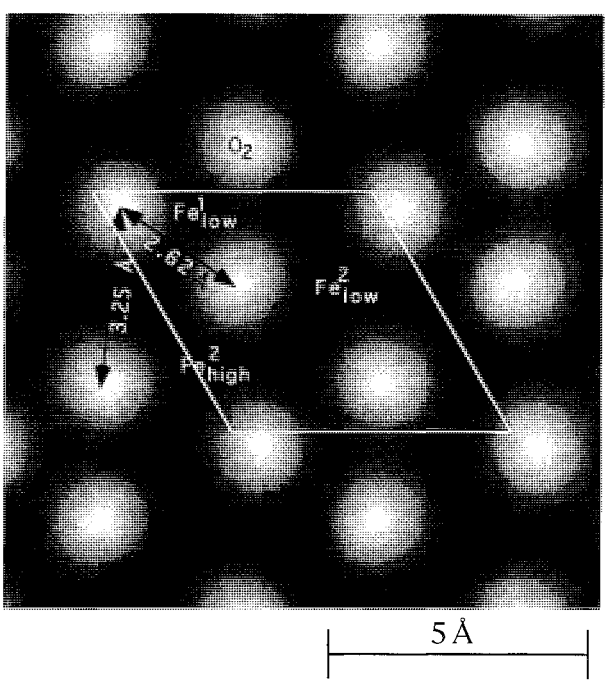

FIGURE 13. Calculated STM image of a hematite {001} surface with adsorbed O_2 (see Fig. 3), at -0.3 V bias voltage. Distances between bright spots vary from 2.62 to 3.25 Å, which is not in agreement with the experimentally observed uniform spot-spot separation of 2.95 Å (see Fig. 5).

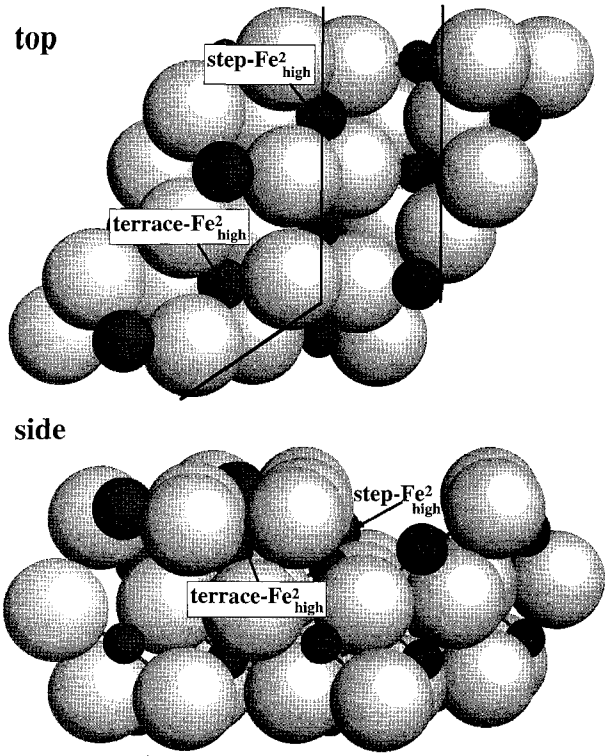

FIGURE 14. Top and side views of a hematite 2 × 2 surface supercell that was used to model the electronic structure of a step. Two Fe_2O_3 units were removed (outlined by two lines in the top-view model) to create a groovelike structure. Only the surface relaxation of flat terraces was applied, but because of computational expense, no surface relaxation was included that is specific for the steps shown. The side view represents the actual thickness of the slab used for the calculations. The slab is infinite perpendicular to the [001] axis (e.g., infinite to the left, right, top, and bottom in the top view). The labels "step" and "terrace" in the top view represent two Fe^2_{high} atoms underneath a flat terrace and at a step edge.

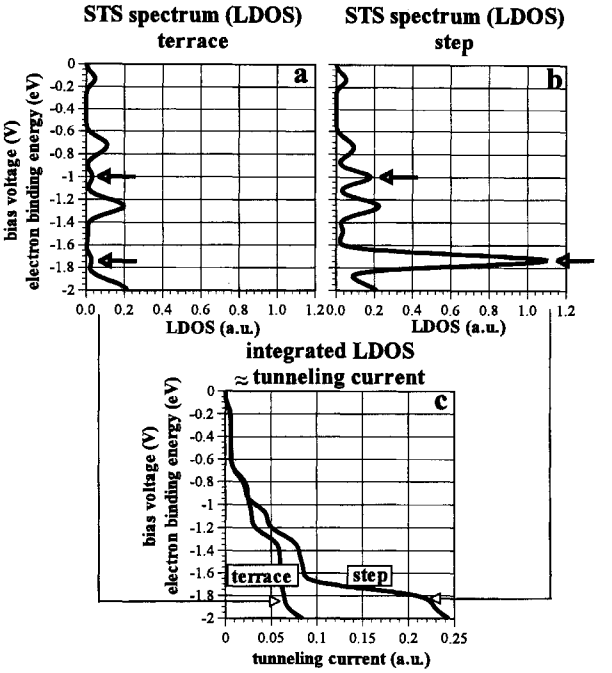

FIGURE 15. Calculated STS spectra with tip positions above Fe^2_{high} atoms underneath a flat terrace (**a**) and at a step edge (**b**) (see also Fig. 14). Both spectra show peaks at similar positions, but there are two peaks in the step spectrum (**b**) that are almost absent in the terrace spectrum (**a**) (marked by arrows). These result in the increase in valence-band density observed in the experimental STM image (Fig. 4). (**c**) Integrated LDOS for these two tip positions, which is roughly proportional to the tunneling current for a given bias voltage and tip position.

the optimized adsorbed structures shown in Figures 2 and 3, respectively. In both images, the major contribution to bright spots comes from O 2p-like states of the adsorbed molecules. Their local density of states at tip positions a few angstroms away from the sample exceeds the LDOS of Fe 3d states because the O atoms of H_2O and O_2 are approximately 2 and 3 Å, respectively, closer to the tip than Fe^1_{low}. Note that in Figure 12, one can also "see" the hydrogen bonds as brighter shades between the egg-like structures that represent H_2O molecules.

Neither of these images can reproduce the experimentally observed uniform spot-spot separation of 2.95 Å. In addition, at positive bias voltages, each of these adsorbed structures would show three bright spots per unit cell almost equally spaced, which is not in agreement with any of the images shown in Figure 9. This is additional evidence that the observed STM images are indeed mimicking fresh surfaces.

It can be assumed that the observed STM images do not represent adventitious C even though we did not specifically calculate this. The binding energy of adsorbed CO_2 would be too low because it does not have a permanent dipole moment, in contrast to H_2O that interacts with the highly ionic hematite surface forming hydrogen bonds (Fig. 2), and CO_2 cannot be polarized as easily as O_2. In addition, adventitious C in a lower oxidation state than the C in CO_2 is not likely to form such a regular pattern with uniformly distributed bright spots that are exactly 2.95 Å apart.

Electronic structure near step sites

To examine differences in the electronic structure of step and terrace sites, we created a 2 × 2 surface unit cell from which two surface Fe_2O_3 units were removed. In this way, a "groove" was created (Fig. 14) that mimics the atomic structure of an atomic surface step. Because of the computational cost of such a setup, a slightly less expensive basis set had to be applied (the diffuse part of the Fe 3d set was contracted into the inner valence part) and no geometry optimization was performed near the step site. Only the surface relaxation as derived from flat surfaces was taken into account. Therefore, only a qual-

itative comparison of calculated STS spectra with tip positions above step and terrace Fe atoms is possible where the Fe atoms are otherwise equivalent on flat terraces (Fe^2_{high} in Fig. 15). Even though the STS spectra of the terrace (Fig. 15a) and the step Fe atoms (Fig. 15b) show certain similar features, the calculated STS spectrum above the step Fe atom has two significant peaks at −1.0 and −1.7 eV (marked by arrows in Fig. 15) that are much lower for the STS spectrum above the terrace site. Projections of these spectra onto Fe 3d, Fe 4s, and O 2p orbitals (analogous to Fig. 8) show that these peaks in the step spectrum have predominantly Fe 3d–O 2p antibonding character with a minor contribution from Fe 4s–O 2p bonding character. Because of the differences in the terrace and step spectra, one would expect an increase in tunneling intensity at step sites for images taken at a negative bias voltage, this effect being even more pronounced from −1.0 V on. To quantify this effect, Figure 15c represents the integral over the LDOS, which is roughly proportional to the tunneling current at a particular bias voltage. With this information, one would expect the tunneling current to be about 15% higher at step sites (hidden by the line width in Fig. 15c) for bias voltages in the range between 0 and −1.1 V. For bias voltages between −1.1 and −1.6 V, a tunneling current increase at step sites of about 50% is expected with respect to equivalent sites on terraces, and an increase of about a factor of 3 is expected at −2 V. Therefore, the calculated spectra nicely explain the experimentally observed increase in electronic density at step sites in Figure 4. In addition, they hint at why the reactivity at these sites is significantly different from the reactivity on terraces (Junta and Hochella 1994), because typically the top 3 eV of the valence band is involved in reactions that require electron transfer (e.g., Luther 1990).

Acknowledgments

We thank Kevin Rosso, Eric Rufe, Carrick Eggleston, Kathy Nagy, and an anonymous reviewer for their reviews of the manuscript and Gotthard Szabo and Jack Tossell for getting us started with the molecular orbital calculations. Technical support by the computing center of the Virginia Polytechnic Institute and State University, in particular by Ray Stell and Randy Marchany, is much appreciated. The research was supported by grant EAR-9305031 from the National Science Foundation and by the Petroleum Research Fund of the American Chemical Society (28720-AC2). E.A. was supported by a fellowship administered by the Associated Western Universities–Northwest Division under grant DE-FG06-89ER-75522 with the U.S. Department of Energy (CAS).

References cited

Avouris, P., and Lyo, I. (1991) Probing and inducing surface chemistry with the STM: The reactions of Si(111)-7 × 7 with H_2O and O_2. Surface Science, 242, 1–11. Becker, U. (1995a) Program to optimize basis sets and geometries using the periodic HF approach Crystal92 (publicly available). Department of Geological Sciences, Virginia Polytechnic Institute and State University, Blacksburg.

———(1995b) Programs to calculate STM images, STS spectra and XPS spectra using Crystal92 and Gaussian94 (publicly available). Department of Geological Sciences, Virginia Polytechnic Institute and State University, Blacksburg.

———(1995c) The electronic structure of galena and hematite surfaces: Applications to the interpretations of STM images, XPS spectra and heterogeneous surface reactions, 189 p. Ph.D. dissertation, Virginia Polytechnic Institute and State University, Blacksburg.

Becker, U., and Hochella, M.F., Jr. (1996) The calculation of STM images, STS spectra and XPS peak shifts for galena: New tools for understanding mineral surface chemistry. Geochimica et Cosmochimica Acta, 60, 2413–2426.

Catti, M., Valerio, G., and Dovesi, R. (1995) Theoretical study of electronic, magnetic, and structural properties of α-Fe_2O_3 (hematite). Physical Review B, 51, 7441–7450.

Causà, M., Dovesi, R., Pisani, C., and Roetti, C. (1988) Ab initio characterization of the (0001) and (10$\bar{1}$0) crystal faces of α-alumina. Surface Science, 215, 259–271.

Ciccacci, F., and De Rossi, S. (1991) Empty electron states in Fe_2O_3 by ultraviolet inverse-photoemission spectroscopy. Physical Review B, 44, 10444–10448.

Condon, N.G., Murray, P.W., Leibsle, F.M., Thornton, G., Lennie, A.R., and Vaughan, D.J. (1994) Fe_3O_4(111) termination of α-Fe_2O_3(0001). Surface Science, 310, L609–L613.

Dovesi, R., Saunders, V.R., and Roetti, C. (1994) Crystal92: An ab-initio Hartree-Fock LCAO program for periodic systems. University of Turin, Italy.

Drager, G., Czolbe, W., and Leiro, J.A. (1992) High-energy-spectroscopy studies of a charge-transfer insulator: X-ray spectra of α-Fe_2O_3. Physical Review B, 45, 8283–8287.

Eggleston, C.M., and Hochella, M.F., Jr. (1992) The structure of hematite {001} surfaces by scanning tunneling microscopy: Image interpretation, surface relaxation, and step structure. American Mineralogist, 77, 911–922.

Eggleston, C.M., Sulzberger, B., and Stumm, W. (1992) Tunneling and force-distance spectroscopy of mineral surface electronic and electrostatic structure. 203rd American Chemical Society, National Meeting. Abstracts of Papers, 203, GEOC 67.

Eggleston, C.M., and Stumm, W. (1993) Scanning tunneling microscopy of Cr(III) chemisorbed on α-Fe_2O_3(001) surfaces from aqueous solution: Direct observation of surface mobility and clustering. Geochimica et Cosmochimica Acta, 57, 4843–4850.

Fujimori, A., Saeki, M., and Kimizuka, N. (1986) Photoemission satellites and electronic structure of Fe_2O_3. Physical Review B, 34, 7318–7328.

Fujimori, A., Kimizuka, N., Taniguchi, M., and Suga, S. (1987) Electronic structure of Fe_3O. Physical Review B, 36, 6691–6694.

Hay, P.J., and Wadt, W.R. (1985) Ab initio effective core potentials for molecular calculations: Potentials for main group elements Na to Bi. Journal of Chemical Physics, 82, 270–283.

Hendewerk, M., Salmeron, M., and Somorjai, G.A. (1986) Water adsorption on the (001) plane of Fe_2O_3: An XPS, UPS, AUGER, and TPD study. Surface Science 172, 544–556.

Henrich, V.E., and Cox, P.A. (1994) The surface science of metal oxides, 464 p. Cambridge University Press, Cambridge, U.K.

Hering, J.G., and Stumm, W. (1990) Oxidative and reductive dissolution of minerals. In Mineralogical Society of America Reviews in Mineralogy, 23, 427–466.

Hochella, M.F., Jr. (1990) Atomic structure, microtopography, composition, and reactivity of mineral surfaces. In Mineralogical Society of America Reviews in Mineralogy, 23, 87–132.

———(1994) Mineral surfaces: Their characterization and their chemical, physical and reactive nature. In D.J. Vaughan and R.A.D. Pattrick, Eds., Mineral surfaces, p. 17–60. Mineralogical Society Series, Chapman and Hall, London, U.K.

Junta, J.L., and Hochella, M.F., Jr. (1994) Manganese (II) oxidation at mineral surfaces: A microscopic and spectroscopic study. Geochimica et Cosmochimica Acta, 58, 4985–4999.

Junta-Rosso, J.L., and Hochella, M.F., Jr. (1996) The chemistry of hematite {001} surfaces. Geochimica et Cosmochimica Acta, 60, 305–314.

Kageshima, H., and Tsukada, M. (1992) Theory of scanning tunneling microscopy and spectroscopy on Si(100) reconstructed surfaces. Physical Review B, 46, 6928–6937.

Kawai, J., Suzuki, C., Adachi, H., Konishi, T., and Gohshi, Y. (1994) Charge-transfer effect on the linewidth of Fe Kα X-ray fluorescence spectra. Physical Review B, 50, 11347–11354.

Knocke, W.R., Occiano, S., and Hungate, R. (1990) Removal of soluble

manganese from water by oxide-coated filter media. American Water Works Association Research Foundation, Denver, Colorado.

Kurtz, R.L., and Henrich, V.E. (1983) Geometric structure of the α-Fe_2O_3(001) surface: A LEED and XPS study. Surface Science, 129, 345–354.

———(1987) Surface electronic structure and chemisorption on corundum transition-metal oxides: α-Fe_2O_3. Physical Review B, 36, 3413–3421.

Lad, R.J., and Henrich, V.E. (1989a) Determination of valence states in Fe_3O_4 by resonant photoemission. Journal of Vacuum Science & Technology A, 7, 1893–1897.

———(1989b) Photoemission study of the valence-band electronic structure in FeO, Fe_3O_4, and α-Fe_2O_3 single crystals. Physical Review B, 39, 13478–13485.

Latajka, Z., and Scheiner, S. (1989) Dissection of basis set superposition error at SCF and correlated levels: HF dimer. Theochem, 58, 9–22.

Lennie, A.R., Condon, N.G., Leibsle, F.M., Murray, P.W., Thornton, G., and Vaughan, D.J. (1996) Structures of Fe_3O_4(111) surfaces observed by scanning tunneling microscopy. Physical Review B, 53, 10244–10253.

Lovlie, R. (1993) Experimental determination of the relationship between magnetic moment and grain geometry of PSD magnetite grains. Physics of the Earth and Planetary Interiors, 76, 105–112.

Luther, G.W. (1990) The frontier-molecular orbital theory approach in geochemical processes. In W. Stumm, Ed., Aquatic chemical kinetics, p. 173–198. Wiley, New York.

Manassidis, I., De Vita, A., and Gillan, M.J. (1993) Structure of the (0001) surface of αAl_2O_3 from first principles calculations. Surface Science Letters, 285, L517–L521.

Masai, J., Shibata-Seki, T., Seki, K., Mori, K., Yamauchi, H., Sasaki, K., Yoshiyama, R., and Yamamoto, M. (1994) Surface characterization of flexible magnetic disk with scanning probe microscopy. Journal of Vacuum Science & Technology B, 12, 1881–1885.

Pisani, C., Dovesi, R., and Roetti, C. (1988) Hartree-Fock ab initio treatment of crystalline systems. Lecture Notes in Chemistry, 193 p. Springer-Verlag, Berlin.

Sato, Y., and Akimoto, S. (1979) Hydrostatic compression of four corundum type compounds: α-Al_2O_3, V_2O_3, Cr_2O_3, and α-Fe_2O_3. Journal of Applied Physics, 50, 5285–5291.

Sherman, D.M. (1985) The electronic structures of Fe cubed + coordination sites in iron oxides: Applications to spectra, bonding and magnetism. Physics and Chemistry of Minerals, 12, 161–175.

Sherman, D.M., and Waite, T.D. (1985) Electronic spectra of Fe^{3+} oxides and oxide hydroxides in the near IR to near UV. American Mineralogist, 70, 1262–1269.

Tasaki, A., and Iida, S. (1963) Magnetic properties of synthetic single crystal of α-Fe_2O_3. Journal of the Physical Society of Japan, 18, 1148–1154.

Tersoff, J., and Hamann, D.R. (1985) Theory of the scanning tunneling microscope. Physical Review B, 31, 805–813.

Tossell, J.A., Vaughan, D.J., and Johnson, K.H. (1973) Electronic structure of ferric iron octahedrally coordinated to oxygen. Eos, 54, 504.

———(1974) The electronic structure of rutile, wustite, and hematite from molecular orbital calculations. American Mineralogist, 59, 319–334.

Tossell, J.A., and Vaughan, D.J. (1992) Theoretical geochemistry: Application of quantum mechanics in the earth and mineral sciences, 514 p. Oxford University Press, Oxford, U.K.

Towler, M.D. (1993) The BILLY Program. Theoretical Chemistry Department, University of Bristol, U.K.

Tsukada, M., Kobayashi, K., Isshiki, N., and Kageshima, H. (1991) First principles theory of scanning tunneling microscopy. Surface Science Reports, 13, 265–304.

Vaughan, D.J., and Tossell, J.A. (1978) Major transition-metal oxide minerals: Their electronic structures and the interpretation of mineralogical properties Canadian Mineralogist, 16, 159–168.

Williams, W., Hoffmann, V., Heider, F., Goeddenhenrich, T., and Heiden, C. (1992) Magnetic force microscopy imaging of domain walls in magnetite. Geophysical Journal International, 111, 417–423.

Worlton, T.G., Bennion, R.B., and Brugger, R.M. (1967) Pressure dependence of the Morin transition in α-Fe_2O_3 to 26 kbar. Physics Letters, 24A, 653–655.

Zeng-Jun, Z., and Jun-Jue, Y. (1992) Sputtering iron oxide films by a water vapor process. Journal of Magnetism and Magnetic Materials, 115, 87–98.

MANUSCRIPT RECEIVED OCTOBER 23, 1995
MANUSCRIPT ACCEPTED JULY 1, 1996